Anatomy of the tsunami and Lamb waves-induced ionospheric signatures generated by the 2022 Hunga Tonga volcanic eruption

Edhah Munaibari[1], Lucie M Rolland[2], Anthony Sladen[3], and Bertrand Delouis[4]

[1]Université Côte d'Azur, Observatoire de la Côte d'Azur, CNRS, IRD, Géoazur
[2]Géoazur, Observatoire de la Côte d'Azur, Université de Nice Sophia Antipolis
[3]Geoazur
[4]University of Nice - Sophia Antipolis CNRS/IRD

January 20, 2023

Abstract

As tsunamis propagate across open oceans, they remain largely unseen due to the lack of adequate sensors, hence limiting the scope of existing tsunami warnings. A potential alternative method relies on the Global Navigation Satellites Systems to monitor the ionosphere for Traveling Ionospheric Disturbances created by tsunami-induced internal gravity waves (IGWs). The approach has been applied to tsunamis generated by earthquakes but rarely by undersea volcanic eruptions injecting energy into both the ocean and the atmosphere. The large 2022 Hunga Tonga-Hunga Ha'apai volcanic eruption tsunami is thus a challenge for tsunami ionospheric imprint detection. Here, we show that in near-field regions (<1500km), despite the complex wavefield, we can isolate the tsunami imprint. We also highlight that the eruption-generated Lamb wave's ionospheric imprints show an arrival time and an amplitude spatial pattern consistent with internal gravity wave origin.

Anatomy of the tsunami and Lamb waves-induced ionospheric signatures generated by the 2022 Hunga Tonga volcanic eruption

E. Munaibari[1], L. Rolland[1], A. Sladen[1], B. Delouis[1]

1 – Université Côte d'Azur, Observatoire de la Côte d'Azur, CNRS, IRD, Géoazur, 250 rue Albert Einstein, Sophia Antipolis 06560 Valbonne, France, edhah.munaibari@geoazur.unice.fr

Key points:

- The tsunami of the 2022 Hunga Tonga-Hunga Ha'apai volcanic eruption triggered ionospheric imprints across the Pacific Ocean
- The eruption produces high ionospheric noise, especially in the near field, making its tsunami ionospheric imprints harder to identify
- The ionospheric imprints of the eruption-triggered Lamb wave are consistent with internal gravity waves origin

Abstract

As tsunamis propagate across open oceans, they remain largely unseen due to the lack of adequate sensors, hence limiting the scope of existing tsunami warnings. A potential alternative method relies on the Global Navigation Satellites Systems to monitor the ionosphere for Traveling Ionospheric Disturbances created by tsunami-induced internal gravity waves (IGWs). The approach has been applied to tsunamis generated by earthquakes but rarely by undersea volcanic eruptions injecting energy into both the ocean and the atmosphere. The large 2022 Hunga Tonga-Hunga Ha'apai volcanic eruption tsunami is thus a challenge for tsunami ionospheric imprint detection. Here, we show that in near-field regions (<1500km), despite the complex wavefield, we can isolate the tsunami imprint. We also highlight that the eruption-generated Lamb wave's ionospheric imprints show an arrival time and an amplitude spatial pattern consistent with internal gravity wave origin.

Plain Language Summary

To complement conventional tsunami warning systems, it is possible to rely on the imprint of the tsunami in the ionosphere, a high-altitude layer of the atmosphere. This imprint can be tracked using the Global Navigation Satellites Systems to measure the Total Electron Content (TEC) of the ionosphere. On Jan. 15, 2022, the submarine volcano of Hunga Tonga-Hunga Ha'apai erupted, providing a unique opportunity to test the approach on a tsunami generated by a volcanic eruption. Here, we study the tsunami's ionosphere response, the pressure pulse the eruption generated, and the underlying physical mechanisms. We find that the eruption caused a particularly high ionosphere activity in the near-field region, making the tsunami signature assessment and use for early-warning more challenging but still possible.

1. Introduction

Tsunamis are natural hazards that have already claimed the lives of more than 250000 civilians globally (Mizutori & Guha-Sapir, 2018). Tsunamis are commonly monitored on shores by coastal tide gauges or in deep oceans by tsunami buoys. These instruments provide direct measurements of the tsunami but can be insufficient for early warnings because (1) tide gauges are located on the coasts, giving little to no time for a warning, and (2) tsunami buoys are expensive to deploy and maintain, resulting in a limited sampling of the oceans, not sufficient for near-field warning. An alternative but indirect method centers around the computation of the ionospheric total electron content (TEC) to track tsunami propagation. The first tsunami-induced ionospheric (TEC) signature was presented by Artru et al. (2005), and since, this technique has been used to identify and characterize the TEC signatures of a variety of tsunamis, all initiated by submarine earthquakes (Liu et al., 2006; Rolland et al.,2010; Galvan et al., 2011; Grawe & Makela, 2015, 2017). Underwater volcanic eruptions and landslides can also trigger tsunamis, except that there haven't been many large instances in the last decades to study them in the light of modern instrumentation. The 2022 explosion of the Hunga Tonga-Hunga Ha'apai (HTHH) submarine volcano provides a unique opportunity to fill this gap and characterize the generated ionospheric perturbations.

According to the US Geological Survey (USGS), the HTHH volcano (20.546°S 175.39°W; Fig. 1a) violently erupted on Jan. 15, 2022, at 4:14:45 UTC (17:14:45 LT). The eruption released a massive ash plume that reached an altitude of ∼55 km (Smart 2022). It also generated a highly-energetic atmospheric Lamb wave observed globally (for a few days after the eruption) in different types of measurements (e.g., barometers, infrasound sensors, satellites images, ionospheric measurements) (Matoza et al.,2022; Wright et al., 2022). According to Themens et al. (2022), large and medium-scale traveling ionospheric disturbances (TIDs) appeared in global TEC measurements following the eruption, with travel speeds ranging from 200 to 1000 m/s. They attributed the two TIDs types to the initial acoustic response of the explosive eruption and the energetic Lamb wave, respectively. The same findings were reported by Lin et al. (2022). In addition, Astafyeva et al. (2022) used the nearfield TEC measurements to identify the presence of several volcanic explosions during the event timeline. Moreover, the eruption triggered air-sea (tsunami-like) waves induced by the Lamb-wave-sea coupling and observed worldwide (Kubota et al., 2022; Omira et al., 2022). According to Matoza et al. (2022), the Lamb wave signature appears to be consistent (arrival time, waveform) in both the ionospheric and sea-level observations.

The eruption also produced a classical tsunami, i.e., from direct water mass displacement, detected across the Pacific Ocean (Carvajal et al., 2022), causing four casualties in Tonga (Latu, 2022) and two in Peru (Parra, 2022). The exact mechanism triggering the tsunami is not well-understood yet, but preliminary analysis suggests a combination of submarine explosion and caldera collapse (Hu et al., 2022 and reference therein). An ionospheric imprint of this tsunami was reported by Matoza et al. (2022) at near-field. Here, we strengthen the study with a spatial pattern analysis and expand the investigated dataset more globally (Pacific-wide). We seek to isolate the ionospheric signature of the tsunami from the acoustic and Lamb signals. Because of these multiple, partially overlapping signals, we don't expect the discrimination to be straightforward, yet, it is a necessary step to assess the potential of TEC data for tsunami early-warning even in the case of a volcanic eruption.

To support our TEC signal analysis, we first analyze the ionospheric imprint of a tsunami initiated by the Mw 8.1 Kermadec earthquake, which occurred a year before, on March 4th, 2021 about 1000 km South of Tonga (29.723°S 177.279°W, based on the USGS report) (Fig. 1a). Both events occurred in the Eastern region of Polynesia islands sparsely equipped with GNSS stations installed onland. The size of the tsunami triggered by the Kermadec earthquake was smaller than the one triggered by the HTHH event by less than one order of magnitude (respectively 3 and 20 cm in the near-field after Romano et al., 2021 and Lynett et al., 2022). We thus use the Kermadec ionospheric imprints as a test case to help decipher the HTHH imprints in the ionosphere with a sparse multi-GNSS network.

In addition to presenting the ionospheric imprints of the two tsunamis, we investigate how the tsunami generation mechanism (earthquake vs. volcano) affects the detection of such imprints. We compare the tsunami sea-level variations to the ionosphere imprints to confirm the tsunami origin of the detected ionospheric imprints. Finally, we examine the ionospheric response of the Lamb wave the HTHH eruption produced and compare it to that of the tsunami.

2. Data and methods

The previous detections of tsunami-induced ionospheric imprints in the literature are based on the use of dense networks of GNSS receivers (Grawe & Makela, 2017 and references therein). Here, the sparsity of GNSS receivers in the south Pacific area requires a single receiver approach to identify the tsunami's ionospheric response and study its evolution at various distances and directions. To test the single receiver technique, we examine the Kermadec tsunami through the GNSS receiver located in Niue Island (NIUM; Fig. 1a), ~1400 km from the epicenter. Such distance favors the detection of both the earthquake and the tsunami ionospheric signatures (Fig. 1a). While the coseismic acoustic gravity wave (AGW) can be observed next to the source, the ionospheric imprint of the IGW triggered by the tsunami cannot appear closer than 500 km from the source and sooner than 1h after the initiation because the atmospheric wave also needs to propagate vertically at a speed below 100 m/s (Occhipinti et al., 2013). For tsunami early-warning, these properties make the AGW measurements more suited in the near-field (Zedek et al., 2021) and the tsunami-induced IGW measurements more suited in the medium and far-field (this study).

From the NIUM GNSS observation data, we compute the raw slant total electron content (sTEC) and apply a sequence of filters (polynomial detrend, apodization, and band-pass filter; see S1 & S2 in SM for a detailed description). The bottom panel of Figure 2a depicts the raw sTEC observed by the satellite-receiver pair G12-NIUM. The top x-axis in the panel indicates the satellite elevation where we applied a mask removing data below 20° elevation (unlike the 10° mask adopted for the rest of this work) to minimize the possible artifacts enhanced by the low elevation (see G12 in Figure 3a). After that, we use the theoretical tsunami travel times (TTT) to estimate the expected tsunami arrival time at a particular location (e.g., sTEC data IPPs location: the intersection of the line of sight with the ionosphere shell at a certain altitude [Davies & Hartmann, 1997], 300km in this study), knowing that the associated TEC signature should appear approximately around the same time (Rolland et al., 2010). These processing steps allow us to observe two distinct signatures: the earthquake acoustic response (A1) appearing ~10 min after the initiation time (IT) and the tsunami (T1) emerging within the expected arrival time. This pattern is consistent over the different satellites seen by the receiver (Fig. 3a). The spatial pattern of the imprints' maximum TEC amplitude around the receiver further assesses the detection. According to Grawe & Makela (2015), the TEC amplitude of tsunami-induced IGWs increases from upstream to downstream the receiver (Fig. 3c). The technique's applicability is made possible thanks to multi-GNSS observations with an efficient azimuthal coverage that increases the reliability of the detection.

We follow the same procedure for the HTHH tsunami, selecting GNSS receivers located in several Pacific islands (Fig. 1a; Table S3 in SM), to extend our analysis with more global coverage. The detection made by each receiver is independent of the others. We selected receivers with multi-GNSS capability. The chosen receivers fall in a distance ranging from 700 km to 10 000 km, and thus from near to far field, with respect to the tsunami source. This allows us to track the fully-developed tsunami in the ionosphere as it travels across the Pacific.

3. Results

1. Tsunami-induced TEC signatures across the Pacific Ocean

We identified the ionospheric imprints of the HTHH tsunami in the TEC data from 12 receivers around the Pacific (Fig. 1b). The tsunami-induced ionospheric imprints are corroborated by observations from other satellites for each receiver (Fig. S5 to S15 in SM). The tsunami TEC amplitude and the local tsunami arrival time of the twelve series are illustrated in Table S3 of the SM. These results agree with the dense-network-based study of Ravanelli et al., in review GRL, 2022 (specifically in the vicinity of New Caledonia and New Zealand).

Applying our detection method with the GNSS receiver located on Lord Howe Island (LORD; Fig. 1a) during the generation and passage of the HTHH tsunami, we successfully identified its ionospheric signatures, as confirmed by the two-step verification procedure (Fig. 3b,d). By comparing the Kermadec and HTHH signatures (Fig. 2a,b), we see how exceptional the HTHH event is; a complex time series with imprints of multiple types of waves, and an amplitude one order of magnitude larger (Table S3 in SM).

2. Ionospheric imprints comparison (earthquake-induced vs. volcanic eruption-induced)

To investigate the impact of the trigger source (earthquake vs. volcanic eruption) on the induced ionospheric signatures of a tsunami, we focus on two TEC measurements with optimal configuration (the orientation of the tsunami aligns with the local geomagnetic field, and the observing geometry is downstream the receivers; Grawe & Makela, 2015): G12-NIUM (Kermadec; Fig. 2a) and C01-TUVA (HTHH; Fig. 2b). Both are located in the medium field (∼1400 km) and are band-pass filtered from 0.7 to 10 mHz.

For the Kermadec event, we observe two remarkable signatures that we link to the event. The first signature is the earthquake acoustic response appearing several minutes after the initiation as an N-shape pulse, as routinely observed after earthquakes. We have strong arguments supporting that the second signature is that of the tsunami: (1) it occurs within the expected arrival time of the tsunami, (2) it has an oscillatory signature with a clear frequency peak at 1.2 mHz, in the range of what is expected for the tsunami waves, (3) it is supported by the different satellites seen by the receiver (Fig. 3a), and (4) the IGWs behavior of the detected signatures' maximum TEC amplitude (Fig. 3c).

Unlike the Kermadec submarine earthquake, the HTHH submarine volcanic eruption ionospheric imprints are more complex and present a richer spectrum. Besides the tsunami response (T1) and the signature of the initial acoustic response (A1), a Lamb wave (L1) is visible in the volcano eruption data. The two types of imprints (excluding the tsunami's) are reported by Wright et al. (2022). The imprint of the tsunami emerges at the expected arrival time with an amplitude of 0.58 TECU. In contrast to the earthquake case, the ionosphere during the eruption experiences higher noise related to the main, massive, explosion of the eruption, and the numerous different types of waves it injected into the Earth's atmosphere (Wright et al., 2022). Such noise can also be seen in some of the sTEC series shown in Figure 1 (see also Fig. 3b), especially those close to the volcano.

3. Ionosphere vs. sea-level measurements

To further assess the tsunami origin of the identified imprints, we compared the sTEC disturbance measured offshore Galapagos Islands with the sea-level anomaly registered by a deep-sea DART buoy #32413 about 800 km southwest of the Islands (Fig. 1a). Both signals have similar waveforms with a peak frequency around 1.2 mHz (Fig. 4a). The emergence of the signal 30 minutes earlier in the ionosphere suggests that the shoaling of the bathymetry around the Galapagos archipelago slowed down the tsunami in the sea surface while allowing its induced IGWs to advance ahead of it. A similar effect was observed for the 2011 Tohoku tsunami when it approached Hawaii (Occhipinti et al., 2011).

We also note the presence of an ionospheric signature having an amplitude and a spectral content similar to the tsunami imprint but 2 hours earlier (Fig. 4a). It appears to travel with a speed of ~235 m/s and could be the imprint of an IGW triggered by the eruption and traveling all the way in the atmosphere.

4. Ionospheric imprints of the Lamb wave

When examining the ionospheric (TEC) data as we search for the HTHH tsunami imprints, we first notice the peculiar signature of the Lamb wave, whose raw sTEC measurements display massive decreases and increases that resemble a large W-shape (Fig. S16 in SM). The Lamb wave processed imprints exhibit close similarity to the tsunami's. We note that the ionospheric signature of both the Lamb and the tsunami waves peak at a similar frequency of 1.2 mHz (Fig. 2b), with the Lamb wave displaying a more impulsive behavior. Furthermore, Figure 2e shows that the Lamb wave's imprint' maximum sTEC amplitude spatial pattern exhibits IGW behavior (similar to the tsunamis cases in Figures 2c and 2d), where the maximum amplitude is larger downstream of the GNSS receiver. Overall, the Lamb wave signature has a larger amplitude than the tsunami signature.

We also investigated the co-located measurements of a DART buoy's Lamb wave pressure signature and its ionospheric signature in southern New Zealand (Fig. 4b). They both show an impulsive waveform (in the time domain) and a broadband frequency content (Fig. 4b). In addition, when corrected for traveled distances, the imprints show no delay between the arrival at the buoy's location and the ionosphere and are consistent with the Lamb wave constant speed (318m/s). The amplitude pattern and absence of time delay suggest that in the same way as the tsunami, the Lamb wave triggered internal gravity waves (IGW), which traveled upward to ionospheric heights with the same horizontal speed as the Lamb wave.

4. Discussion

The global overview of the ionospheric imprint amplitude shows interesting features (Fig. 1). The tsunami's smallest sTEC amplitude is observed in Hawaii. Three possible reasons could have caused the lower amplitude aside from the tsunami open-ocean size itself (∼6 cm zero to crust recorded by the 51407 DART buoy): (1) the local time of the tsunami arrival was around 1 am (Table S3), meaning a low ionization rate (compared to the daytime) and consequently a smaller amplitude of detected signatures (Grawe & Makela, 2015), (2) the inefficient coupling between the tsunami-induced IGWs and the local geomagnetic field, or (3) the destructive interaction between the conjugate Traveling Ionospheric Disturbances (TIDs) and the direct TIDs traveling away from the volcano as suggested by Themens et al. (2022). This later scenario is based on the fact that Hawaii is very close to the volcano's geomagnetic conjugate point. Lin et al. (2022) also reported the presence of conjugate TIDs, lending more support to this explanation.

In contrast, the tsunami ionospheric signature with the largest amplitude in the vicinity of the Galapagos Islands suggests a tsunami with a higher open-ocean wave (∼6 cm zero to crust recorded by the 32413 DART buoy), which contradicts the expected wave height decay with increasing distance from the source (∼2 cm; model) (Ward 2002). Unlike the other identified imprints, the detection near the Galapagos took place around noon local time (Table S3 in SM), which contributes to the larger amplitude of the detected ionospheric imprints.

The lack of delay between the arrival of the Lamb wave imprints in the ionosphere and on the surface, as illustrated by Figure 4b, suggests that the propagation of the Lamb acts like a moving source (similar to a tsunami), forcing IGWs that travels obliquely upward (Lin et al., 2022). The IGW behavior experienced by the imprints' max sTEC amplitude (depicted in Figure 3e) supports such a hypothesis.

5. Conclusions

The ionospheric imprints of the tsunami generated by Jan. 15, 2022, Hunga Tonga-Hunga Ha'apai volcanic eruption, as it propagates across the Pacific Ocean, are presented and investigated along with that of the Mar. 4, 2021, 8.1 Mw Kermadec Islands earthquake tsunami. Our results indicate that, like the ionospheric imprints of earthquake-initiated tsunamis, the imprints of the tsunami generated by the HTHH eruption can be identified and isolated in the ionospheric data, even with a single station approach. This result was achieved despite a high level of ionospheric noise, especially in near-field, produced by the volcanic eruption. This noise complexifies the detection of tsunami-induced ionospheric imprints, calling for further improvement in the filtering algorithms and differentiation criteria in order to meet the high detection confidence required for early warnings. Yet, the comparison with open-ocean sea-level measurements confirmed that the isolated imprints were those of the tsunami.

Our joint analysis of the ionospheric signatures of the Lamb (pressure) and tsunami waves shows that they both trigger internal gravity waves that can be distinguished thanks to their different traveling speeds. Detecting the HTHH tsunami's ionospheric imprints across the Pacific Ocean demonstrates the potential of our single-receiver approach. Its current implementation requires a visual inspection to validate the identified imprints. This absence of automation presents a limitation that we intend to overcome in future work along with utilizing detected tsunami-induced ionospheric signatures to estimate the open-ocean tsunami's wave height, which is the quantity of interest to tsunami early warning systems.

Data and Resources

All GNSS data are freely available from the Geoscience Australia data archives (ftp://ftp.data.gnss.ga.gov.au/daily/) and the CDDIS data archives (https://cddis.nasa.gov/Data_and_Derived_Products/GNSS/daily_30second_data.html). The ocean bathymetry data ETOPO1 (1-minute global relief model; Amante and Eakins 2009) and the open-ocean sea-level measurements (DART) are from the NOAA data archives (https://www.ngdc.noaa.gov/mgg/bathymetry/relief.html; https://www.ngdc.noaa.gov/hazard/DARTData.shtml). The coastal sea-level measurements (tide gauge) are publicly available via the Intergovernmental Oceanographic Commission of UNESCO (http://www.ioc-sealevelmonitor- ing.org/). To generate the tsunami travel times, we take advantage of Geoware TTT SDK software (Wessel, 2009).

Acknowledgement

This work was supported by French Agence Nationale de la Recherche (ANR) under reference ANR-19-CE04- 0003 and Centre national d'études spatiales (CNES) for APR project UVTECGEOX. We thank E. Astafyeva, P. Coïsson, B. Maletckii, F. Manta, D. Mikesell & M. Ravanelli for fruitful discussions within an ad-hoc Geoazur-IPGP-NGI working group on the 2022 Hunga volcano eruption.

References

Amante, C., & Eakins, B.W. (2009). ETOPO1 1 Arc-Minute Global Relief Model: Procedures, Data Sources and Analysis. National Geophysical Data Center, NOAA. https://doi.org/10.7289/V5C8276M

Artru, J., Ducic, V., Kanamori, H., Lognonné, P., & Murakami, M. (2005). Ionospheric detection of gravity waves induced by tsunamis. Geophys. J. Int, 160, 840–848. https://doi.org/10.1111/j.1365-246X.2005.02552.x

Astafyeva, E., Maletckii, B., Mikesell, T. D., Munaibari, E., Ravanelli, M., Coisson, P., Manta, F., & Rolland, L. (2022). The 15 January 2022 Hunga Tonga Eruption History as Inferred From Ionospheric Observations. Geophysical Research Letters, 49(10). https://doi.org/10.1029/2022GL098827

Carvajal, M., Sepúlveda, I., Gubler, A., & Garreaud, R. (2022). Worldwide Signature of the 2022 Tonga Volcanic Tsunami. Geophysical Research Letters, 49(6), 8–11. https://doi.org/10.1029/2022gl098153

Davies, K., & Hartmann, G. K. (1997). Studying the ionosphere with the Global Positioning System. Radio Science, 32(4), 1695–1703. https://doi.org/10.1029/97RS00451

Galvan, D. A., Komjathy, A., Hickey, M. P., & Mannucci, A. J. (2011). The 2009 Samoa and 2010 Chile tsunamis as observed in the ionosphere using GPS total electron content. Journal of Geophysical Research: Space Physics, 116(A6), n/a-n/a. https://doi.org/10.1029/2010JA016204

Grawe, M. A., & Makela, J. J. (2015). The ionospheric responses to the 2011 Tohoku, 2012 Haida Gwaii, and 2010 Chile tsunamis: Effects of tsunami orientation and observation geometry. Earth and Space Science, 2(11), 472–483. https://doi.org/10.1002/2015EA000132

Grawe, M. A., & Makela, J. J. (2017). Observation of tsunami-generated ionospheric signatures over Hawaii caused by the 16 September 2015 Illapel earthquake. Journal of Geophysical Research: Space Physics, 122(1), 1128–1136. https://doi.org/10.1002/2016JA023228

Hu, G., Li, L., Ren, Z., and Zhang, K.: The characteristics of the 2022 Tonga volcanic tsunami in the Pacific Ocean, Nat. Hazards Earth Syst. Sci. Discuss. [preprint], https://doi.org/10.5194/nhess-2022-200, in review, 2022.

Kubota, T., Saito, T., & Nishida, K. (2022). Global fast-traveling tsunamis driven by atmospheric Lamb waves on the 2022 Tonga eruption. Science. https://doi.org/10.1126/science.abo4364

Latu, K. (2022). Prime Minister defends Deputy’s ‘no sirens’ reply as tsunami death toll rises to four. Kaniva Tonga Media. https://www.kanivatonga.nz/2022/01/prime-minister-defends-deputys-no-sirens-reply-as-tsunami-death-toll-rises-to-four/

Lin, J., Rajesh, P. K., Lin, C. C. H., Chou, M., Liu, J., Yue, J., Hsiao, T., Tsai, H., Chao, H., & Kung, M. (2022). Rapid Conjugate Appearance of the Giant Ionospheric Lamb Wave Signatures in the Northern Hemisphere After Hunga-Tonga Volcano Eruptions. Geophysical Research Letters, 49(8). https://doi.org/10.1029/2022GL098222

Liu, J. Y., Tsai, H. F., & Jung, T. K. (1996). Total Electron Content Obtained by Using the Global Positioning System. Terrestrial, Atmospheric and Oceanic Sciences, 7(1), 107. https://doi.org/10.3319/TAO.1996.7.1.107(A)

Lynett, P., McCann, M., Zhou, Z., Renteria, W., Borrero, J., Greer, D., Fa’anunu, O., Bosserelle, C., Jaffe, B., Selle, S. La, Ritchie, A., Snyder, A., Nasr, B., Bott, J., Graehl, N., Synolakis, C., Ebrahimi, B., & Cinar, G. E. (2022). Diverse Tsunamigenesis Triggered by the Hunga Tonga-Hunga Ha’apai Eruption. Nature, 1–22. https://doi.org/10.1038/s41586-022-05170-6

Matoza, R. S., Fee, D., Assink, J. D., Iezzi, A. M., Green, D. N., Kim, K., Toney, L., Lecocq, T., Krishnamoorthy, S., Lalande, J.-M., Nishida, K., Gee, K. L., Haney, M. M., Ortiz, H. D., Brissaud, Q., Martire, L., Rolland, L., Vergados, P., Nippress, A., … Wilson, D. C. (2022). Atmospheric waves and global seismoacoustic observations of the January 2022 Hunga eruption, Tonga. Science. https://doi.org/10.1126/science.abo7063

Mizutori, M., & Guha-Sapir, D. (2018). Economic Losses, Poverty & DISASTERS 1998-2017. Centre for Research on the Epidemiology of Disasters & United Nations Office for Disaster Risk Reduction. Retrieved from https://www.preventionweb.net/files/61119_credeconomiclosses.pdf

Occhipinti, G., Coïsson, P., Makela, J. J., Allgeyer, S., Kherani, A., Hébert, H., & Lognonné, P. (2011). Three-dimensional numerical modeling of tsunami-related internal gravity waves in the Hawaiian atmosphere. Earth, Planets and Space, 63(7), 847–851. https://doi.org/10.5047/eps.2011.06.051

Occhipinti, G., Rolland, L., Lognonné, P., & Watada, S. (2013). From Sumatra 2004 to Tohoku-Oki 2011: The systematic GPS detection of the ionospheric signature induced by tsunamigenic earthquakes. Journal of Geophysical Research: Space Physics, 118(6), 3626–3636. https://doi.org/10.1002/jgra.50322

Omira, R., Ramalho, R.S., Kim, J. et al. Global Tonga tsunami explained by a fast-moving atmospheric source. Nature (2022). https://doi.org/10.1038/s41586-022-04926-4

Parra, N. (2022). Two deaths and tsunami damage reported in Peru: country did not issue an alert. Radio Bío-Bío. https://www.biobiochile.cl/noticias/internacional/america-latina/2022/01/15/reportan-dos-muertes-y-danos-por-tsunami-en-peru-pais-no-emitio-alerta.shtml

Rolland, L. M., Occhipinti, G., Lognonné, P., & Loevenbruck, A. (2010). Ionospheric gravity waves detected offshore Hawaii after tsunamis. Geophysical Research Letters, 37(17). https://doi.org/10.1029/2010GL044479

Romano, F., Gusman, A. R., Power, W., Piatanesi, A., Volpe, M., Scala, A., & Lorito, S. (2021). Tsunami Source of the 2021 M W 8.1 Raoul Island Earthquake From DART and Tide-Gauge Data Inversion . Geophysical Research Letters, 48(17), 1–11. https://doi.org/10.1029/2021gl094449

Smart, D. (2022). The first hour of the paroxysmal phase of the 2022 Hunga Tonga Hunga Ha'apai volcanic eruption as seen by a geostationary meteorological satellite. Weather, 77(3), 81–82. https://doi.org/10.1002/wea.4173

Themens, D. R., Watson, C., Žagar, N., Vasylkevych, S., Elvidge, S., McCaffrey, A., et al. (2022). Global propagation of ionospheric disturbances associated with the 2022 Tonga Volcanic Eruption. *Geophysical Research Letters*, 49, e2022GL098158. doi.org: 10.1029/2022GL098158

Ward, S. (2002). Tsunamis, Encyclopedia of Physical Science and Technology Vol. 17. ed. Meyers, RA, Academic Press, San Diego, 175-191.

Wessel, P. (2009). Analysis of Observed and Predicted Tsunami Travel Times for the Pacific and Indian Oceans. Pure and Applied Geophysics, 166(1–2), 301–324. https://doi.org/10.1007/s00024-008-0437-2

Wright, C.J., et al. (2022) Tonga eruption triggered waves propagating globally from surface to edge of space, *ESSOAr*, https://www.essoar.org/pdfjs/10.1002/essoar.10510674.1

Zedek, F., Rolland, L. M., Mikesell, T. D., Sladen, A., Delouis, B., Twardzik, C., & Coïsson, P. (2021). Locating surface deformation induced by earthquakes using GPS, GLONASS and Galileo ionospheric sounding from a single station. Advances in Space Research, 68(8), 3403–3416. https://doi.org/10.1016/j.asr.2021.06.011

Figure Captions

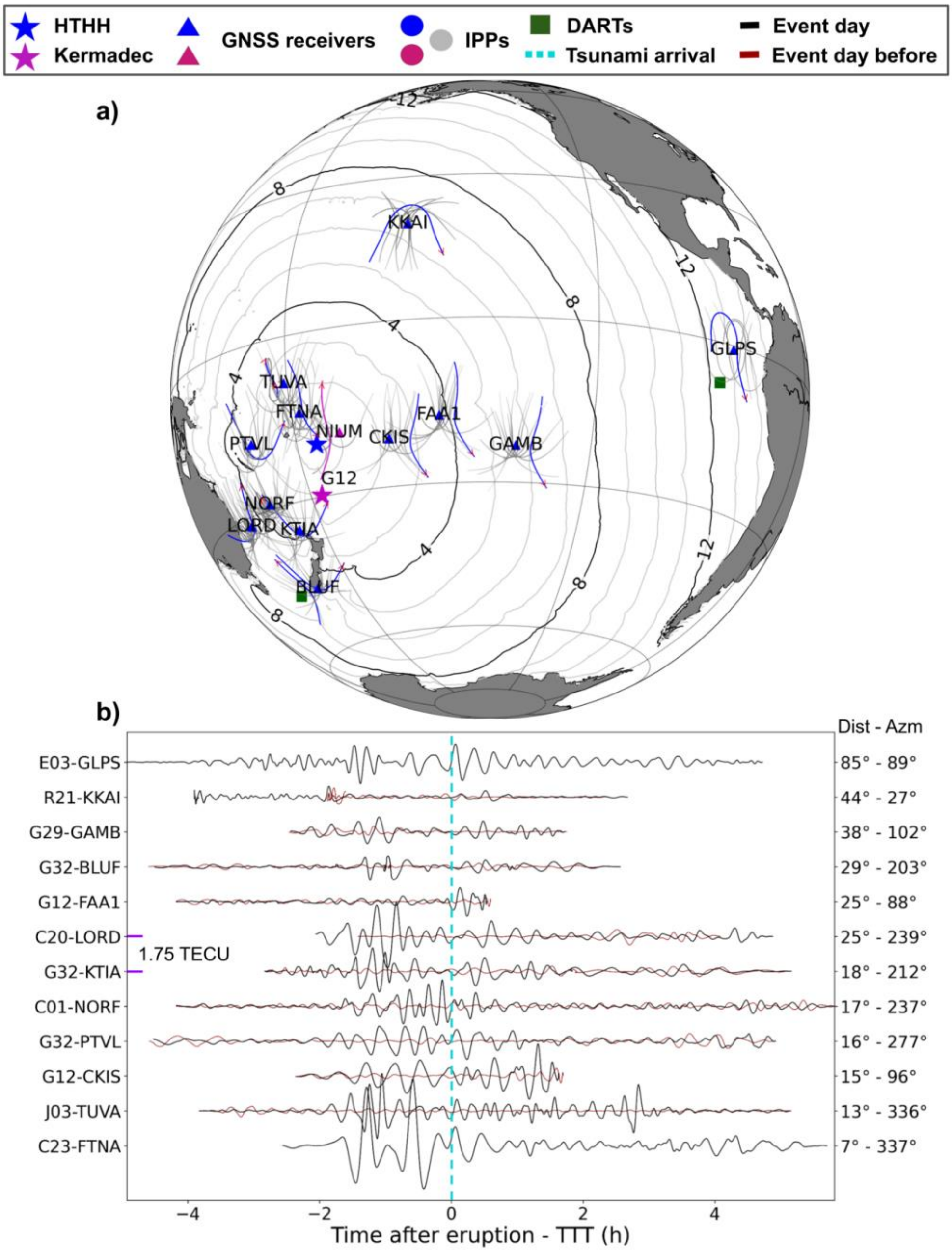

Figure 1. (a) Context map of the study with locations of the tsunami sources and measurements. The Jan. 15, 2022, Hunga Tonga-Hunga Ha'apai volcanic eruption and the Mar. 4, 2021, 8.1 Mw Kermadec Islands earthquake epicenter are marked with a blue and purple star, respectively. GNSS receivers are marked with triangles of the same color. The contours highlight the Hunga theoretical tsunami traveling times (TTT). Ionospheric Pierce Points (IPPs at 300km altitude) are depicted by colored dots for the selected pairs, while gray dots represent that of other pairs. **(b)** A selection of filtered sTEC measurements with tsunami-induced signature. Satellites are marked with a letter: Beidou (C), QZSS (J), GPS (G), GLONASS (R), Galileo (E), and PRN number. To highlight the tsunami signature, the time series are aligned with respect to the tsunami theoretical arrival time (TTT).

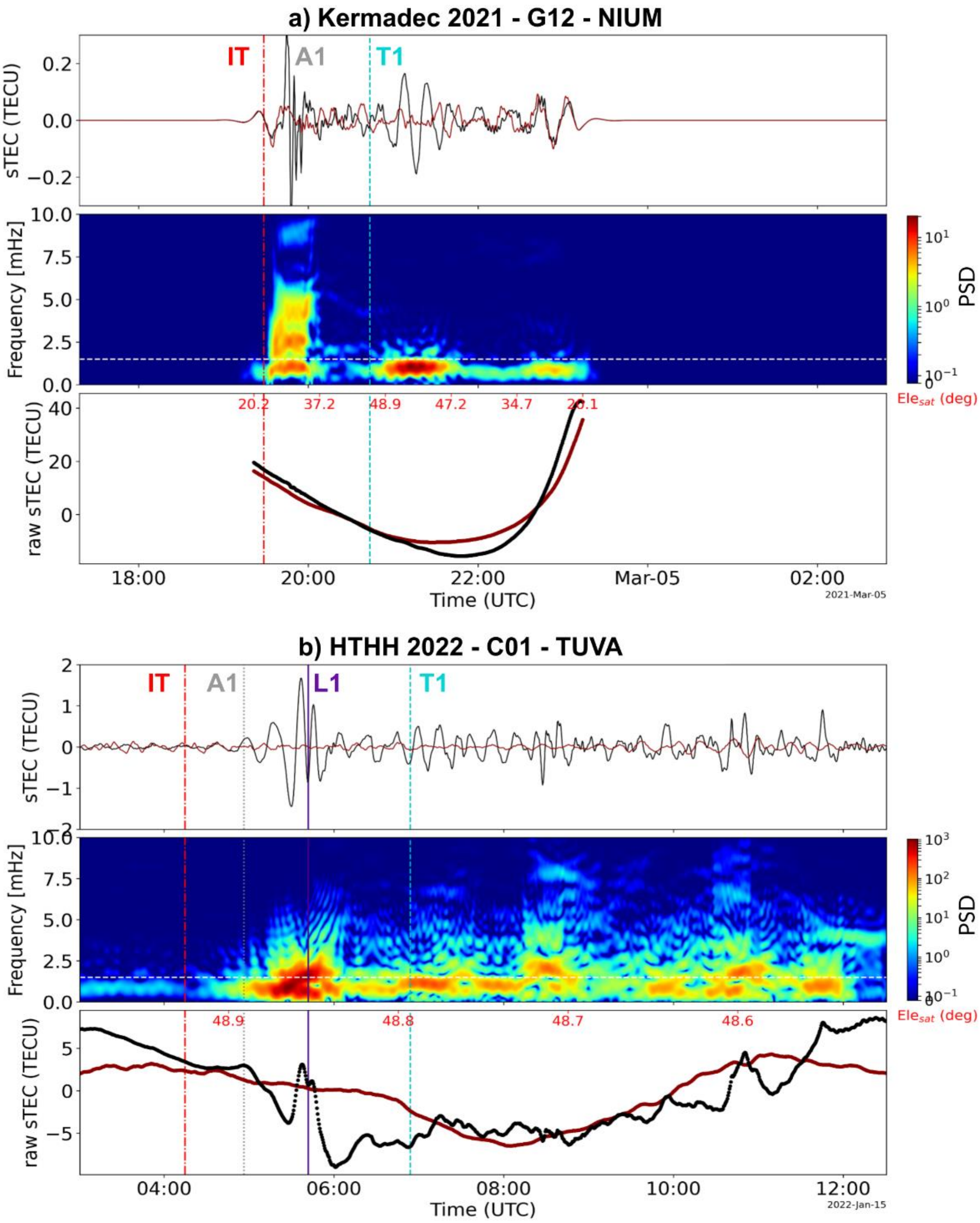

Figure 2. Comparison between the ionospheric TEC imprints obtained by the satellite-receiver pairs G12-NIUM (Kermadec) and C01-TUVA (HTHH). **(a)** TEC measurements during the Kermadec earthquake and the passage of the triggered tsunami. The three panels from bottom to top are: the raw sTEC, the event day filtered sTEC spectrogram, and the filtered sTEC. The filtered sTEC is zero-padded to match the length of C01-TUVA. The vertical red line represents the event initiation time (IT). The top x-axes show the satellite's azimuth and elevation, respectively. The horizontal white line in the spectrogram indicates the expected frequency of tsunami ionospheric signature (i.e., 1.5mHz; 11min). **(b)** TEC measurements during the HTHH volcanic eruption and the produced tsunami passage. The expected arrival times of the acoustic pulse A1; 667m/s, the Lamb wave L1; 318m/s and the tsunami are highlighted.

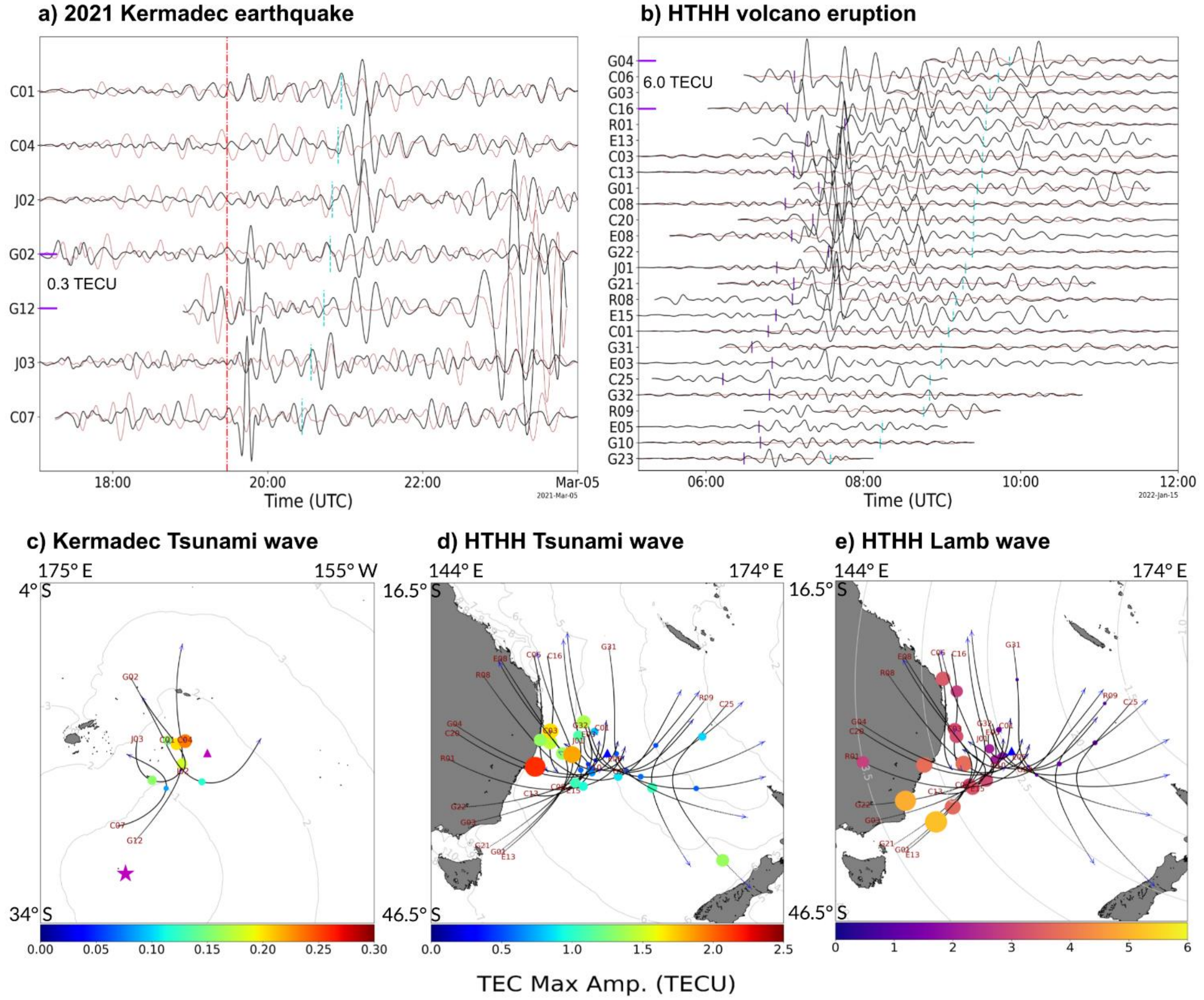

Figure 3. (a) The tsunami-induced ionospheric signatures detected in the vicinity of Niue Island (NIUM) after the 2021 Kermadec earthquake. **(b)** The ionospheric imprints detected in the vicinity of Lord Howe Island (LORD) induced after the HTHH volcanic eruption. **(c)** Geographic view of the earthquake's epicenter, the GNSS receiver, and the ionospheric tracks of the satellites whose sTEC time series are shown in (a). Along the satellites' tracks, the disks indicate the satellites' locations at the tsunami expected arrival time, whose size and color point out the detected maximum sTEC amplitude of the tsunami imprints. The max sTEC amplitude is calculated within a 2-hour observation window starting 15 minutes before TAT as $\frac{max_{obs\_w} - min_{obs\_w}}{2}$. **(d)** Map showing the GNSS receiver and the ionospheric tracks of the satellites whose sTEC time series are shown in (b). **(e)** The disks depicted in the map show the satellites' locations at the Lamb wave arrival, with their size and color representing the wave's maximum sTEC amplitude. The results illustrated by (c), (d), and (e) demonstrate that ionospheric imprints downstream of the receiver display larger max sTEC amp. than upstream, as expected from IGWs.

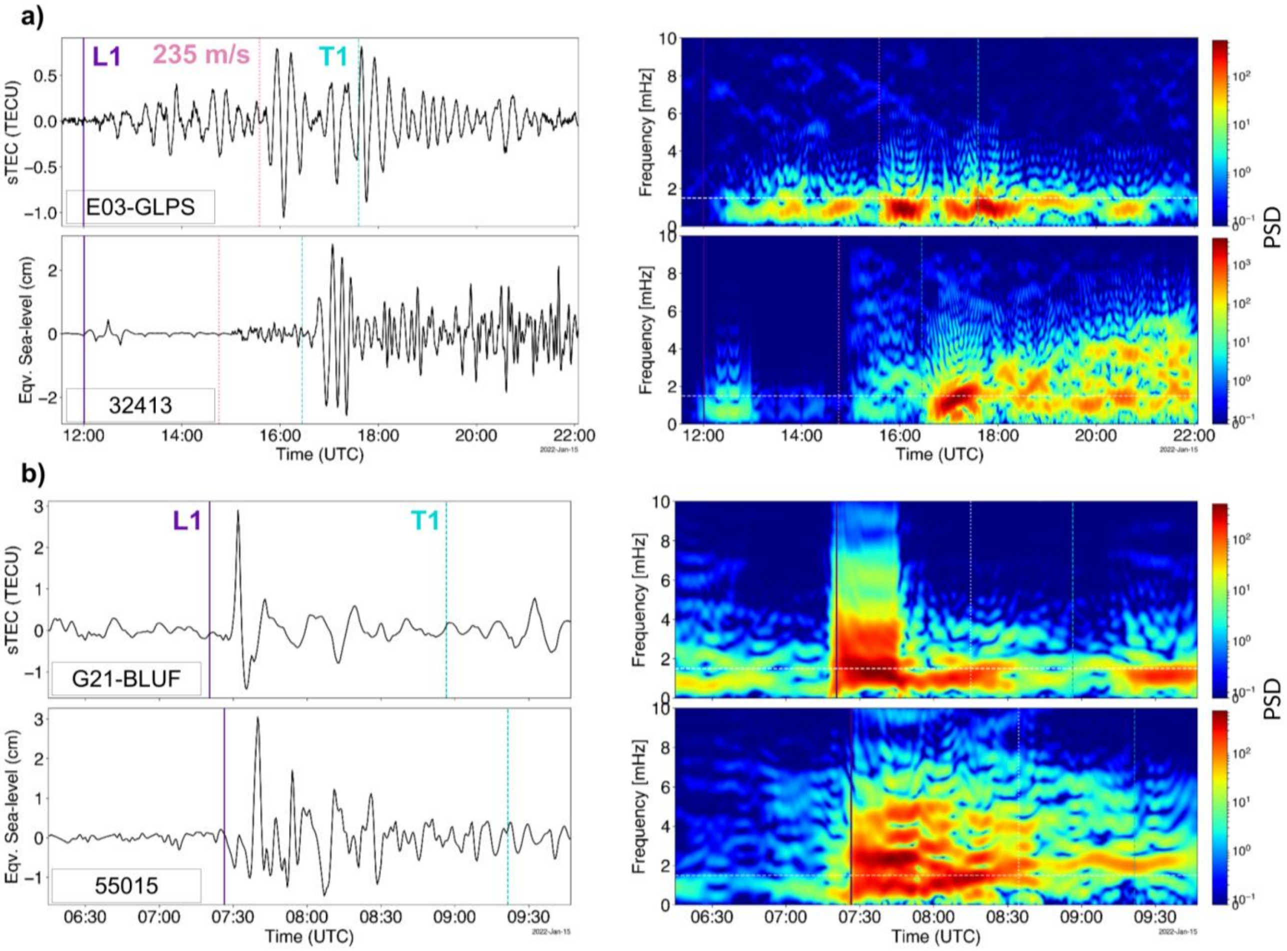

Figure 4. Comparison between open-ocean sea-level anomaly and ionospheric signatures in the vicinity of Galapagos Islands (a) and southern New Zealand (b) on Jan. 15, 2022. Time series are on the left, and spectrograms are on the right. **(a)** The top panel shows the filtered E03-GLPS sTEC measurements. The bottom panel presents the sea-level measurements from the tsunami buoy DART 32413. **(b)** The top panel is the sTEC measurements of G21-BLUF, and the bottom is the sea-level observation of DART 55015. The results show that the Lamb wave is better sensed in the vicinity of southern New Zealand, whereas near the Galapagos Islands, the tsunami is. In addition, the comparison presents a solid confirmation of the origin of each imprint.

Geophysical Research Letters

Supporting Information for

Anatomy of the tsunami and Lamb waves-induced ionospheric signatures generated by the 2022 Hunga Tonga volcanic eruption

E. Munaibari[1], L. Rolland[1], A. Sladen[1], B. Delouis[1]

1 – Université Côte d'Azur, Observatoire de la Côte d'Azur, CNRS, IRD, Géoazur, 250 rue Albert Einstein, Sophia Antipolis 06560 Valbonne, France, edhah.munaibari@geoazur.unice.fr

Contents of this file

Introduction

The supplementary material consists of Text S1 & S2, Table S3 and Figures S4 – S15.

Figure S4 illustrates the slant total electron content (sTEC) processing steps to highlight possible tsunami-generated signatures. The figure is supporting Text S2.

Figure S5 shows the Tonga tsunami ionospheric imprints identified in the vicinity of Wallis & Futuna Islands as detected by FTNA GNSS receiver (a) and the map of the positions of the GNSS receiver and the satellites' ionospheric tracks (b). The figure is supporting the bottom subfigure of Figure 1 in the main text.

Figure S6 presents the Tonga tsunami ionospheric imprints identified in the vicinity of Tuvalu Island as detected by TUVA GNSS receiver (a) and the map of the positions of the volcano, the

GNSS receiver and the satellites' ionospheric tracks (b). The figure is supporting the bottom subfigure of Figure 1 in the main text.

Figure S7 displays the Tonga tsunami ionospheric imprints identified in the vicinity of Cook Islands as detected by CKIS GNSS receiver (a) and the map of the positions of the volcano, the GNSS receiver and the satellites' ionospheric tracks (b). The figure is supporting the bottom subfigure of Figure 1 in the main text.

Figure S8 depicts the Tonga tsunami ionospheric imprints identified in the vicinity of Vanuatu Islands as detected by PTVL GNSS receiver (a) and the map of the positions of the volcano, the GNSS receiver and the satellites' ionospheric tracks (b). The figure is supporting the bottom subfigure of Figure 1 in the main text.

Figure S9 displays the Tonga tsunami ionospheric imprints identified in the vicinity of Norfolk Island as detected by NORF GNSS receiver (a) and the map of the positions of the volcano, the GNSS receiver and the satellites' ionospheric tracks (b). The figure is supporting the bottom subfigure of Figure 1 in the main text.

Figure S10 portrays the Tonga tsunami ionospheric imprints identified in the vicinity of northwest New Zealand as detected by KTIA GNSS receiver (a) and the map of the positions of the volcano, the GNSS receiver and the satellites' ionospheric tracks (b). The figure is supporting the bottom subfigure of Figure 1 in the main text.

Figure S11 shows the Tonga tsunami ionospheric imprints identified in the vicinity of Tahiti as detected by FAA1 GNSS receiver (a) and the map of the positions of the GNSS receiver and the satellites' ionospheric tracks (b). The figure is supporting the bottom subfigure of Figure 1 in the main text.

Figure S12 portrays the Tonga tsunami ionospheric imprints identified in the vicinity of southern New Zealand as detected by BLUF GNSS receiver (a) and the map of the positions of the GNSS receiver and the satellites' ionospheric tracks (b). The figure is supporting the bottom subfigure of Figure 1 in the main text.

Figure S13 depicts the Tonga tsunami ionospheric imprints identified in the vicinity of Gambier Islands as detected by GAMB GNSS receiver (a) and the map of the positions of the GNSS receiver and the satellites' ionospheric tracks (b). The figure is supporting the bottom subfigure of Figure 1 in the main text.

Figure S14 displays the Tonga tsunami ionospheric imprints identified in the vicinity of Hawaii Islands as seen by KKAI GNSS receiver (a) and the map of the positions of the GNSS receiver and the satellites' ionospheric tracks (b). The figure is supporting the bottom subfigure of Figure 1 in the main text.

Figure S15 shows the Tonga tsunami ionospheric imprints identified in the vicinity of Galapagos Islands as detected by GLPS GNSS receiver (a) and the map of the positions of the GNSS receiver and the satellites' ionospheric tracks (b). The figure is supporting the bottom subfigure of Figure 1 in the main text.

Figure S16 depicts raw ionospheric measurements during the eruption of the HTHH volcano to highlight the accompanied massive sTEC decreases and increases that resemble a large W-shape.

All GNSS data are freely available from the Geoscience Australia data archives (ftp://ftp.data.gnss.ga.gov.au/daily/) and the CDDIS data archives (https://cddis.nasa.gov/Data_and_Derived_Products/GNSS/daily_30second_data.html). The ocean bathymetry data ETOPO1 (1-minute global relief model; Amante and Eakins 2009) and the open-ocean sea-level measurements (DART) are from the NOAA data archives (https://www.ngdc.noaa.gov/mgg/bathymetry/relief.html; https://www.ngdc.noaa.gov/hazard/DARTData.shtml). The coastal sea-level measurements (tide gauge) are publicly available via the Intergovernmental Oceanographic Commission of UNESCO (http://www.ioc-sealevelmonitor- ing.org/). To generate the tsunami travel times, we take advantage of Geoware TTT SDK software (Wessel, 2009).

Text S1

TEC, which stands for ionospheric total electron content, is a parameter commonly used to study and investigate the state of the ionosphere (Ratcliffe, 1951a, 1951b), which is the layer containing the ionized part of Earth's upper atmosphere and stretches from approximately 50 km to more than 1000 km. The established definition of the total electron content is the total number of electrons integrated between two points along a column of a meter-squared cross-section according to the following expression

$$TEC = \int n_e(s)\, ds$$

where ds is the integration path and $n_e(s)$ in the location-dependent electron density (Evans, 1957). Before going into how TEC is computed from observations and how it's related to the detection of Tsunamis, a brief look of the theoretical work describing ionospheric disturbances and their driving mechanism is presented.

In 1960, Hines put forward the initial theory describing the cause of ionospheric disturbances. In his theory, Hines (1960) attributed such disturbances to internal atmospheric gravity waves generated in lower regions of the atmosphere and propagated upward to the ionosphere. The theory was then affirmed by the work of Hooke (1969) and Davis (1973) where they studied and analyzed the behavior of electron and ion densities and the integrated ionospheric response (TEC) to internal atmospheric gravity waves, respectively. Within the same time period, it was suggested that surface disturbances such as earthquakes and tsunamis produce internal atmospheric gravity waves (Donn & Posmentier, 1964; Hines, 1972) that travel upward to ionospheric heights imprinting an identifiable signature in the ionosphere. Such suggestion was then expanded upon by Peltier & Hines (1976) where they assessed the different difficulties in detecting the surface disturbances tsunamis ionospheric signature and confirmed the possibility of observing such signature in the TEC.

There are different methods that are developed to obtain ionospheric TEC measurements from observations such as the Faraday Rotation effect on a linear polarized propagating plane wave (Titheridge, 1972). However, today TEC measurements are made mostly using GNSS (Global Navigation Satellite Systems) data. By utilizing the delay imposed by the ionosphere on the signal sent by a satellite, TEC values can be computed. For example, in the case of satellites equipped with dual-frequency systems, the ionospheric delay in meters is found according to

$$I = \frac{40.3\,(f_1^2 - f_2^2)}{f_1^2 f_2^2}\; 10^{16}\, TEC$$

where I can be computed by taking the difference of the two measurements of pseudorange or that of carrier phase obtained by a GNSS receiver station and f_1& f_2 are the two frequencies used by the satellites to transmit signals back to the ground stations (Liu et al., 1996).

The first observation using TEC of an ionospheric signature of a surface disturbance was illustrated by Calais & Minster (1995) for the January 17, 1994, Mw=6.7 Northridge earthquake. As for the ionospheric (TEC) signature of a tsunami, Artru et al. (2005) presented the first observations using the dense Japanese GPS Earth Observation Network (GEONET) for the tsunami generated by the 23 June 2001 earthquake in Peru as it approached Japan. After this pioneering observations, several similar observations were made for other events such as the 26 December 2004 Indian Ocean tsunami (Liu et al., 2006), the 15 November 2006 at Kuril Islands, the 29 September 2009 at Samoa Islands, and the 27 February 2010 at Chile (Rolland et al.,2010).

Text S2

To compute the total electron content (TEC), we use a modified version of GNSS-TEC software (Zhivetiev, 2019). In order to highlight possible tsunami-generated signatures, we process the obtained TEC measurements (Fig. S4). The processing involves the removal of longer period variations in TEC time series (such as diurnal variations and multiple hour trends due to changing elevation angle of the receiver-satellite line of sight) as well as constant receivers/satellites instrumental biases. We carry out the removal by detrending the TEC time series with a polynomial of degree 10 after Galvan et al. (2011) (Fig. S4b), followed by performing apodization with a Hann-window taper to minimize edge effects (Fig. S4c). Then to enhance the tsunami-induced imprints, we apply to the time series a Butterworth band-pass filter with order 3 and frequency limits of 0.7 and 3 mHz (the selection of the filter limits is to encapsulate the range where the frequency of the tsunami waves is expected to be, Rolland et al., 2010) (Fig. S4d). The geolocation of the processed TEC measurements in the ionosphere is based on the thin shell assumption (Davies & Hartmann, 1997). The intersection of the line of sight between a GNSS receiver and a satellite with the ionosphere shell at a certain altitude is known as an ionospheric pierce point or IPP. Within this work, we calculate the IPPs at 300 km altitude as the height of the maximum ionospheric electron density set to be between 200 and 400 km (Zhang et al., 1999).

Table S3: Tsunami TEC amplitude of the ten satellite-receiver pairs ionospheric measurements depicted in Figure 1, along with the local tsunami arrival time at both IPPs' and receivers' locations and ionospheric background activity. The tsunami wave height obtained from the closest tide gauge to each receiver is presented in the last column.

TEC series	Receiver location	Tsunami TEC amplitude (TECU)		Ionospheric background✧ (TECU)	Local tsunami arrival time (TAT)		Tsunami wave height*	
		sTEC	vTEC	vTEC	IPP	GNSS receiver	Height† (m)	Tide gauge code
C23-FTNA	Wallis & Futuna Islands (14.308°S 178.121°W)	0.88	0.49	21.35	2022-01-14 18:04:29	2022-01-15 17:38:41	0.02	wall
J03-TUVA	Tuvalu Island (8.525°S 179.197°E)	0.56	0.34	27.76	2022-01-15 18:54:00	2022-01-15 18:45:22	0.12	fong
G12-CKIS	Cook Islands (21.201°S 159.801°W)	0.97	0.39	25.15	2022-01-14 20:58:29	2022-01-14 20:24:48	0.663	raro
G32-PTVL	Vanuatu Islands (17.749°S 168.315°E)	0.79	0.50	23.76	2022-01-15 18:05:00	2022-01-15 18:19:10	1.006	vanu
C01-NORF	Norfolk Island (29.043°S 167.939°E)	0.67	0.40	21.32	2022-01-15 18:30:30	2022-01-15 19:19:55	1.297	kjni
G32-KTIA	New Zealand (35.069°S 173.273°E)	0.73	0.56	17.51	2022-01-15 19:39:30	2022-01-15 20:28:25	0.692	ncpt
C20-LORD	Lord Howe Island (31.520°S 159.061°E)	0.71	0.51	19.29	2022-01-15 20:24:00	2022-01-15 20:08:11	0.668	gcsb
G12-FAA1	Tahiti (17.555°S 149.614°W)	0.72	0.26	25.97	2022-01-14 22:14:29	2022-01-14 21:53:48	0.296	pape
G32-BLUF	New Zealand (46.585°S 168.292°E)	0.33	0.19	15.17	2022-01-15 19:53:00	2022-01-15 21:39:05	0.107	puyt
G29-GAMB	Gambier Islands (23.130°S 134.965°W)	0.47	0.25	21.32	2022-01-15 01:09:59	2022-01-15 00:45:24	0.227	gamb
R21-KKAI	Hawaii Islands (19.066°N 155.799°W)	0.28	0.12	6.96	2022-01-15 00:56:59	2022-01-15 00:31:01	0.392	hilo2
E03-GLPS	Galapagos Islands (0.743°S 90.304°W)	0.98	0.64	42.81	2022-01-15 11:18:29	2022-01-15 11:18:15	0.864	sant

✧ Values extracted from the archives of Project "Ionospheric Weather" of IZMIRAN: Pushkov Institute of Terrestrial Magnetism, Ionosphere and Radio Wave Propagation Russian Academy of Sciences (https://www.izmiran.ru/ionosphere/weather/)
*Tsunami wave height is obtained from the closest tide gauge station to the GNSS receiver.
†The height is calculated within 6-hour observation window starting 1 hour before TAT as $\frac{max_{obs\_w} - min_{obs\_w}}{2}$, after detrending the raw measurements with polynomial of degree 10.

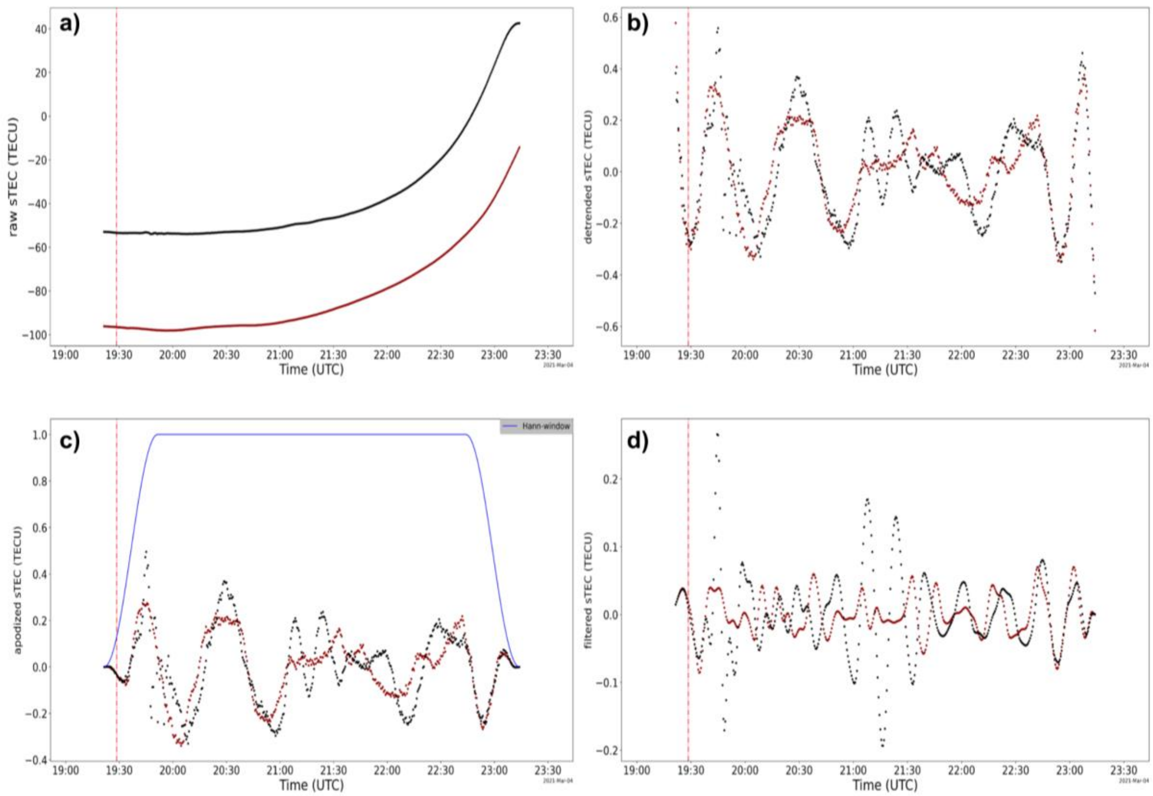

Figure S4. The processing steps of the slant total electron content (sTEC) to highlight possible tsunami-generated signatures: **(a)** raw, **(b)** detrended, **(c)** apodized, and **(d)** band-pass filtered sTEC.

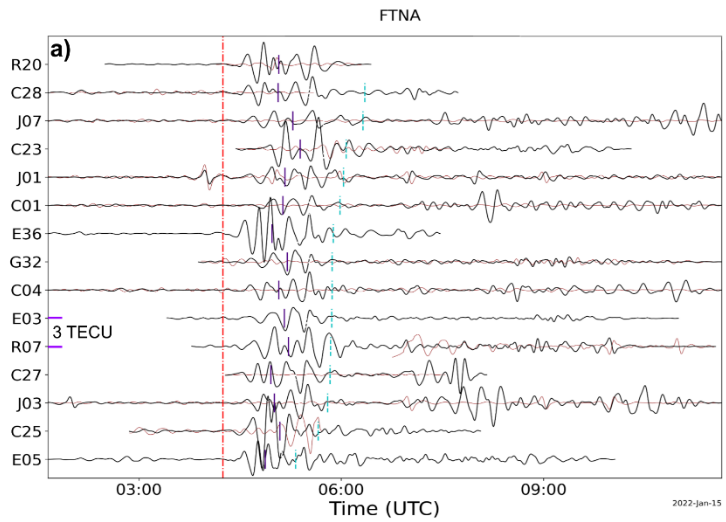

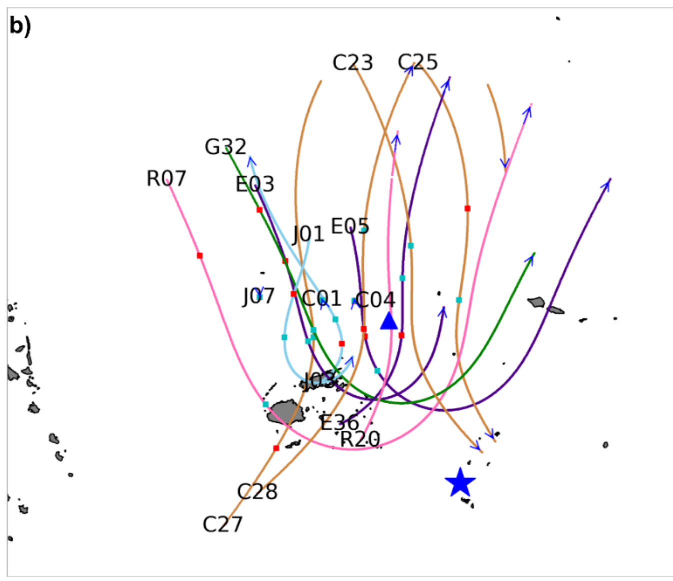

Figure S5. (a) The tsunami-induced ionospheric signatures detected in the vicinity of Wallis & Futuna Islands (FTNA GNSS receiver) following the passage of the tsunami triggered the Jan. 15, 2022 HTHH volcanic eruption. The y axis indicates the satellites ID where the sTEC time series are arranged (bottom to top) according to the tsunami expected arrival time (vertical red dashed lines). The violet vertical solid lines indicate the arrival time of the Lamb (pressure) with traveling speed of 318 m/s, while the vertical green dotted line illustrate the arrival time of a gravity wave (generated by tsunami waves of constant speed as a result of unchanging ocean depth of 5 km) with traveling speed of 221 m/s. **(b)** Geographic view showing the volcano (yellow star), the GNSS receiver (red triangle) and the ionospheric tracks of the satellites (green: GPS, cyan: GLONASS, violet: Galileo, orange: Beidou, skyblue: QZSS) whose sTEC time series are show in (a) with black curves representing the event day data and blue curves denoting that of the day before. Along the satellites' tracks, the pink squares indicate the satellites' locations at the time of the eruption (vertical pink dashdotted line in a), while the red squares point out the satellites' locations at the tsunami expected arrival time (vertical red dashed lines in a). Due to the close proximity to the volcano, the imprints of the tsunami appears to be mixed with that of the other atmospheric waves (e.g. Lamb wave) triggered by the eruption.

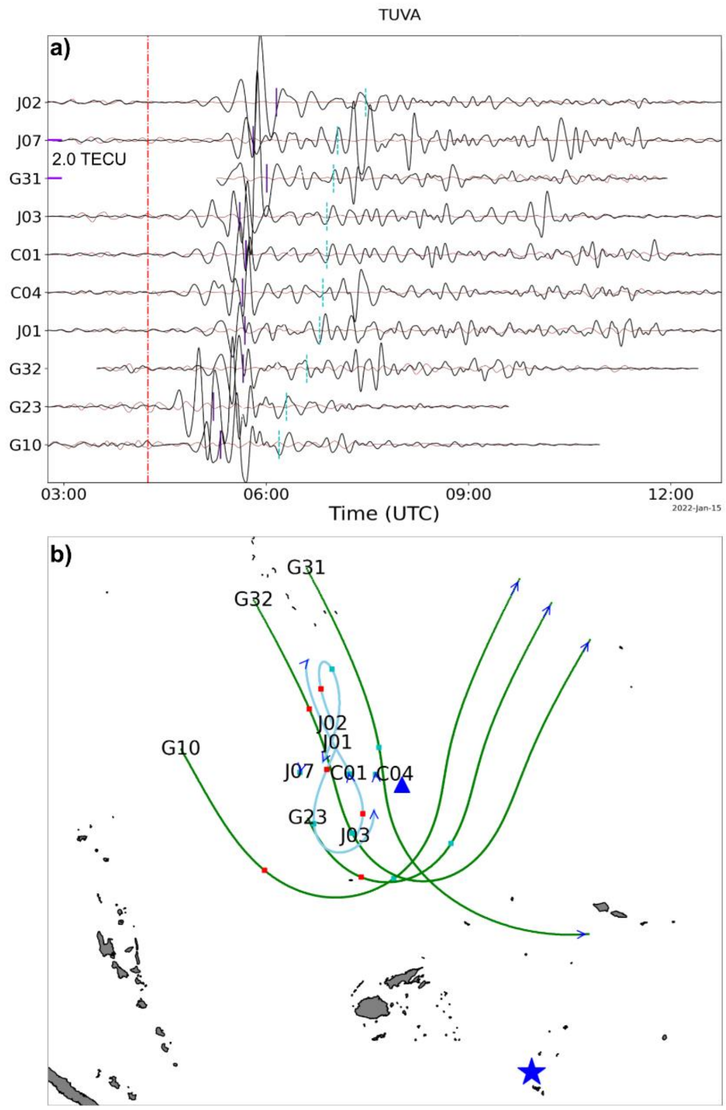

Figure S6. (a) The tsunami-induced ionospheric signatures detected in the vicinity of Tuvalu Island (TUVA GNSS receiver) following the passage of the tsunami triggered the HTHH volcanic eruption. **(b)** Geographic view of the volcano, the GNSS receiver and the ionospheric tracks of the satellites. The ionospheric imprints of the Lamb wave and the tsunami are visible and distinguishable.

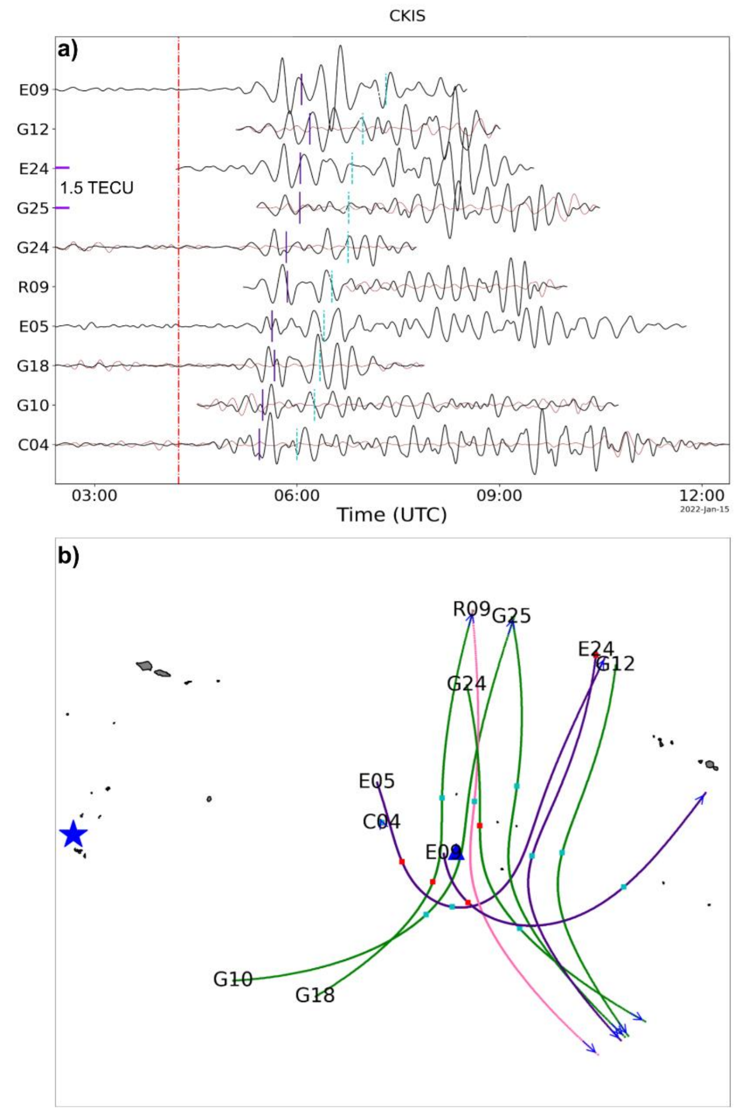

Figure S7. (a) The tsunami-induced ionospheric signatures detected in the vicinity of Cook Islands (CKIS GNSS receiver) following the passage of the tsunami triggered the HTHH volcanic eruption. **(b)** Geographic view of the volcano, the GNSS receiver and the ionospheric tracks of the satellites whose sTEC time series are show in (a). Like the two prior receivers, the ionospheric imprints of the Lamb wave and the tsunami are visible and distinguishable.

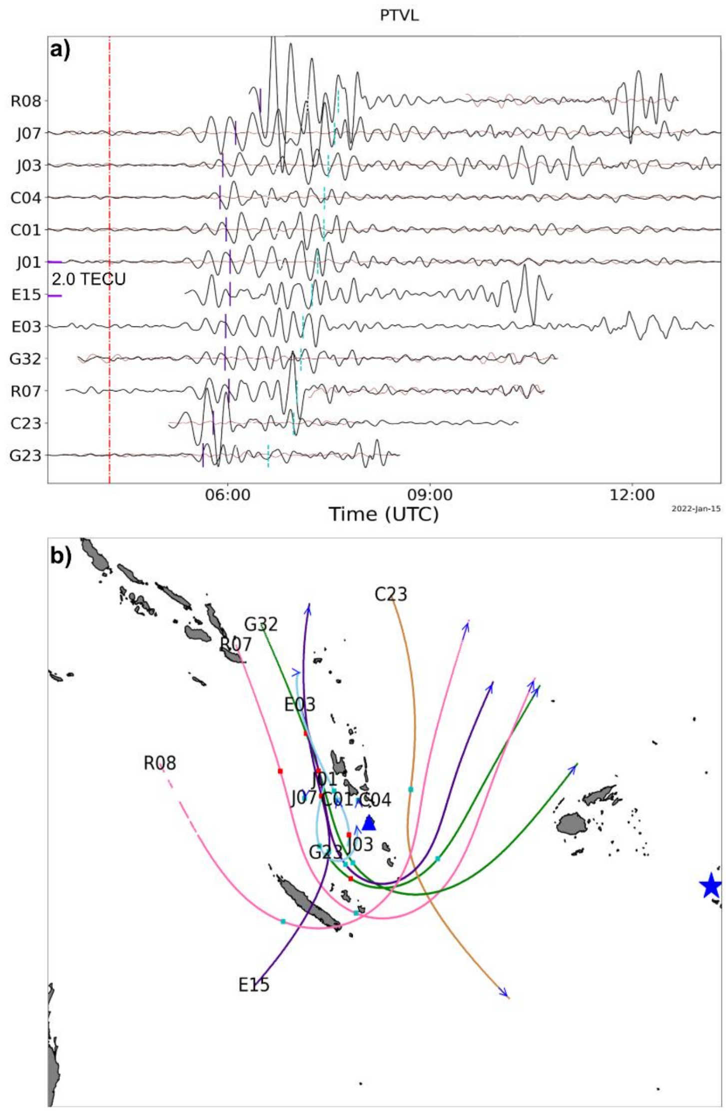

Figure S8. (a) The tsunami-induced ionospheric signatures detected in the vicinity of Vanuatu Islands (PTVL GNSS receiver) following the passage of the tsunami triggered the HTHH volcanic eruption. **(b)** Geographic view of the volcano, the GNSS receiver and the ionospheric tracks of the satellites whose sTEC time series are show in (a). Like the previous cases, we can easily separate the imprints of the Lamb wave from the tsunami's

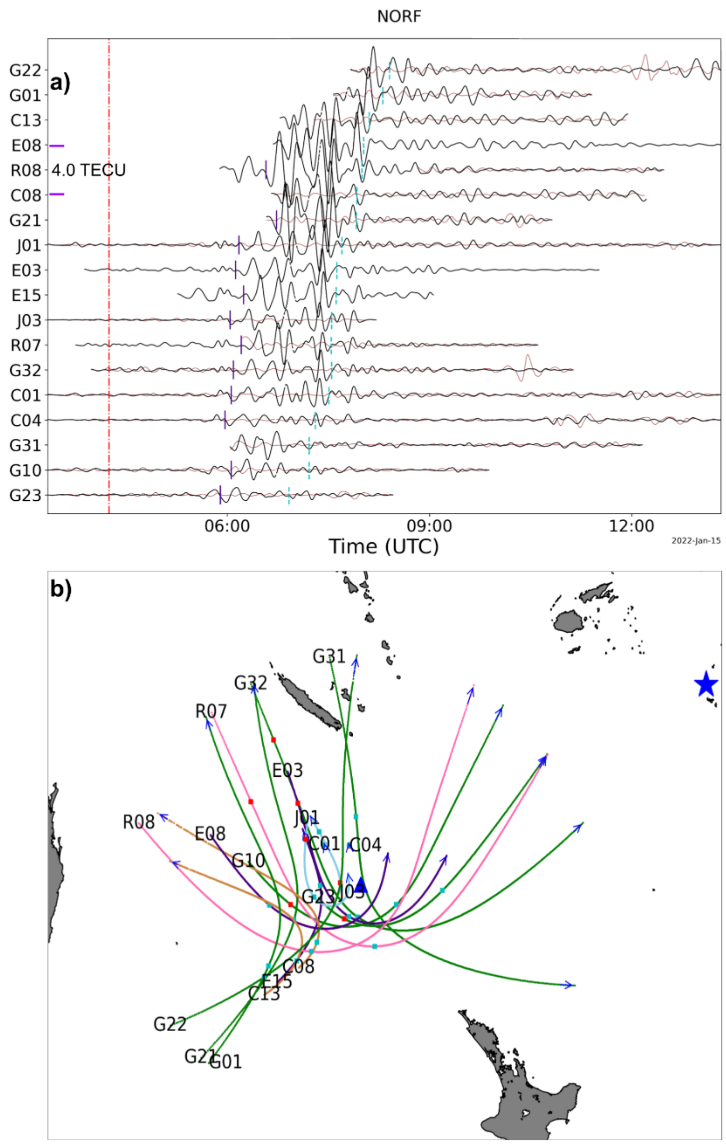

Figure S9. (a) The tsunami-induced ionospheric signatures detected in the vicinity of Norfolk Island (NORF GNSS receiver) following the passage of the tsunami triggered the HTHH volcanic eruption. The eurption time is indicated by the vertical pink dashdotted line. **(b)** Geographic view of the volcano, the GNSS receiver and the ionospheric tracks of the satellites whose sTEC time series are show in (a). One can see clearly the presence of three waves' arrivals; the Lamb wave induced, the constant traveling tsunami induced and the bathymetric tsunami induced.

.

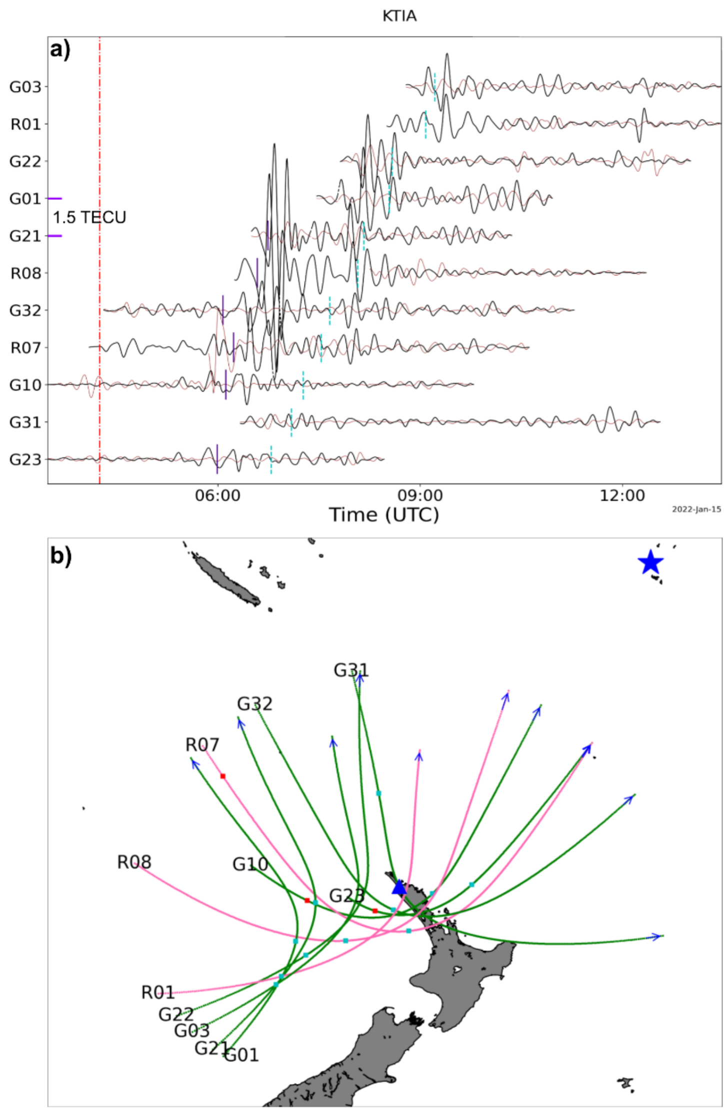

Figure S10. (a) The tsunami-induced ionospheric signatures detected in the vicinity of northwest New Zealand (KTIA GNSS receiver) following the passage of the tsunami triggered the HTHH volcanic eruption. **(b)** Geographic view of the volcano the GNSS receiver and the ionospheric tracks of the satellites whose sTEC time series are show in (a). The results showing here resemble that of PTVL receiver case.

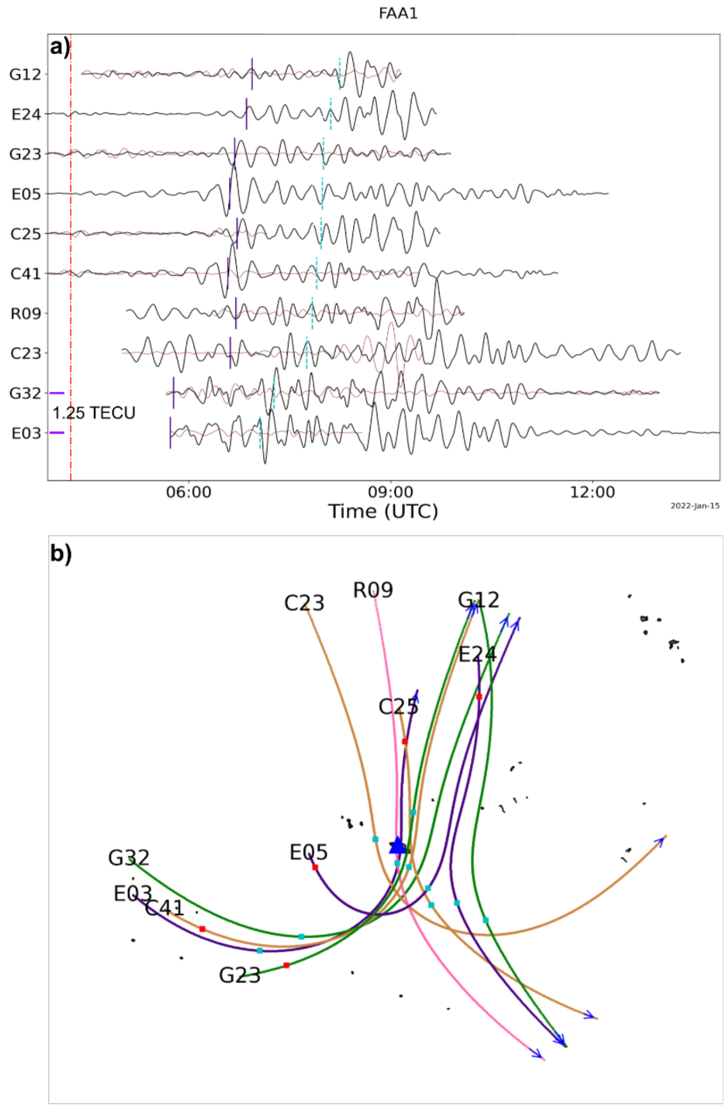

Figure S11. (a) The tsunami-induced ionospheric signatures detected in the vicinity of Tahiti (FAA1 GNSS receiver) following the passage of the tsunami triggered the HTHH volcanic eruption. **(b)** Geographic view of the GNSS receiver and the ionospheric tracks of the satellites whose sTEC time series are show in (a). Due to the distance increase and the different traveling speed of the waves, the tsunami imprints appear to be more visible and less contaminated by the other waves, the eruption injected in the atmosphere.

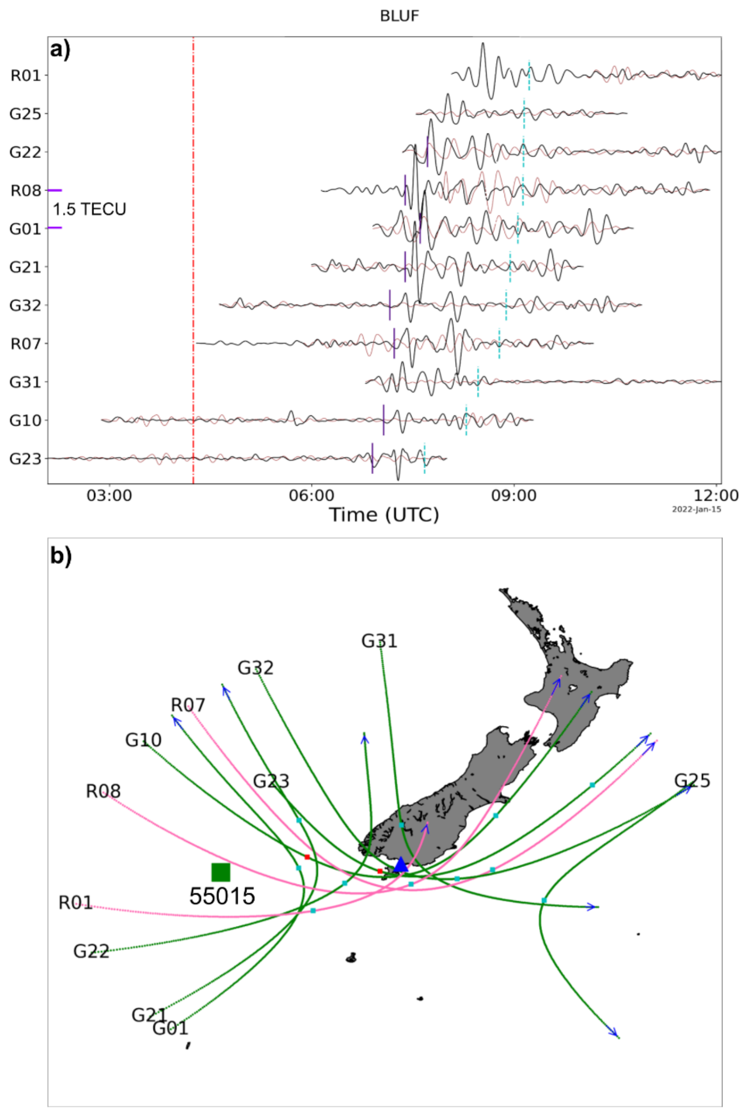

Figure S12. (a) The tsunami-induced ionospheric signatures detected in the vicinity of southern New Zealand (BLUF GNSS receiver) following the passage of the tsunami triggered the HTHH volcanic eruption. **(b)** Geographic view of the GNSS receiver and the ionospheric tracks of the satellites whose sTEC time series are show in (a). Similar to the previous case, the tsunami imprints appear to be more visible and less contaminated by the other waves, the eruption injected in the atmosphere. The black square depicts the position of the tsunami buoy (DART 55015) used in Section 3.4 of the main text.

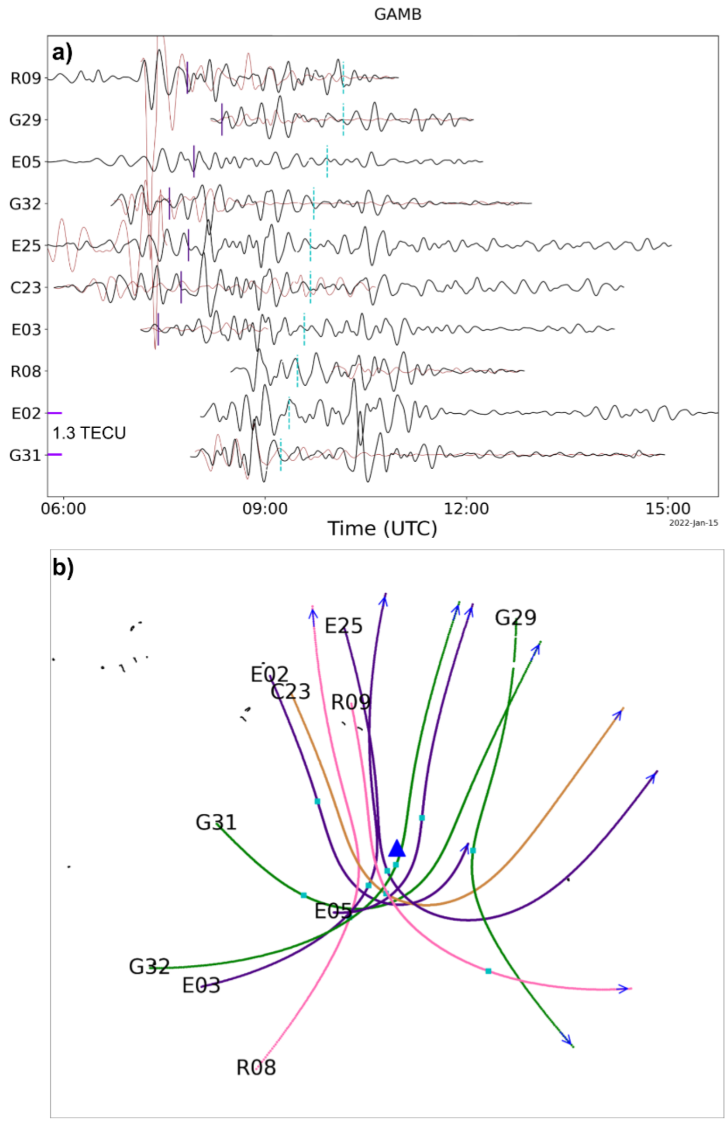

Figure S13. (a) The tsunami-induced ionospheric signatures detected in the vicinity of Gambier Islands (GAMB GNSS receiver) following the passage of the tsunami triggered the HTHH volcanic eruption. **(b)** Map of the GNSS receiver and the ionospheric tracks of the satellites whose sTEC time series are show in (a). With the distance increase, the imprints of the other atmospheric are well separated from that of the tsunami and all appear at their expected times.

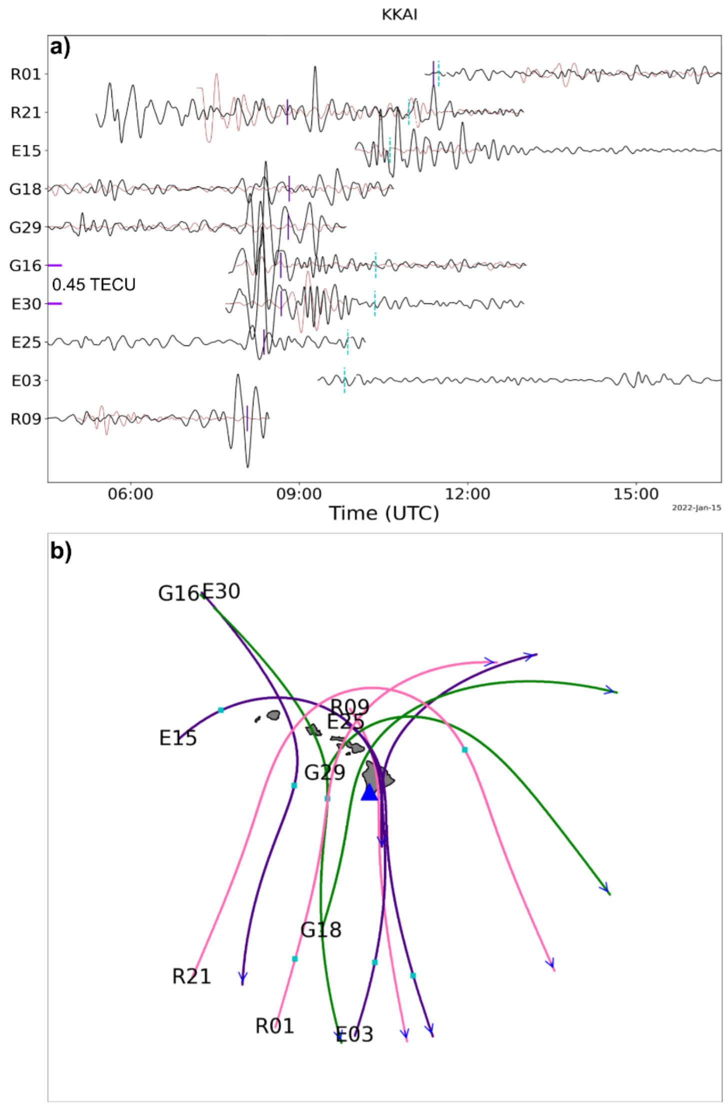

Figure S14. (a) The tsunami-induced ionospheric signatures detected in the vicinity of Hawaii Islands (KKAI GNSS receiver) following the passage of the tsunami triggered the HTHH volcanic eruption. **(b)** Map of the GNSS receiver and the ionospheric tracks of the satellites whose sTEC time series are show in (a). Both the ionospheric signatures of the Lamb wave and the tsunami are visible.

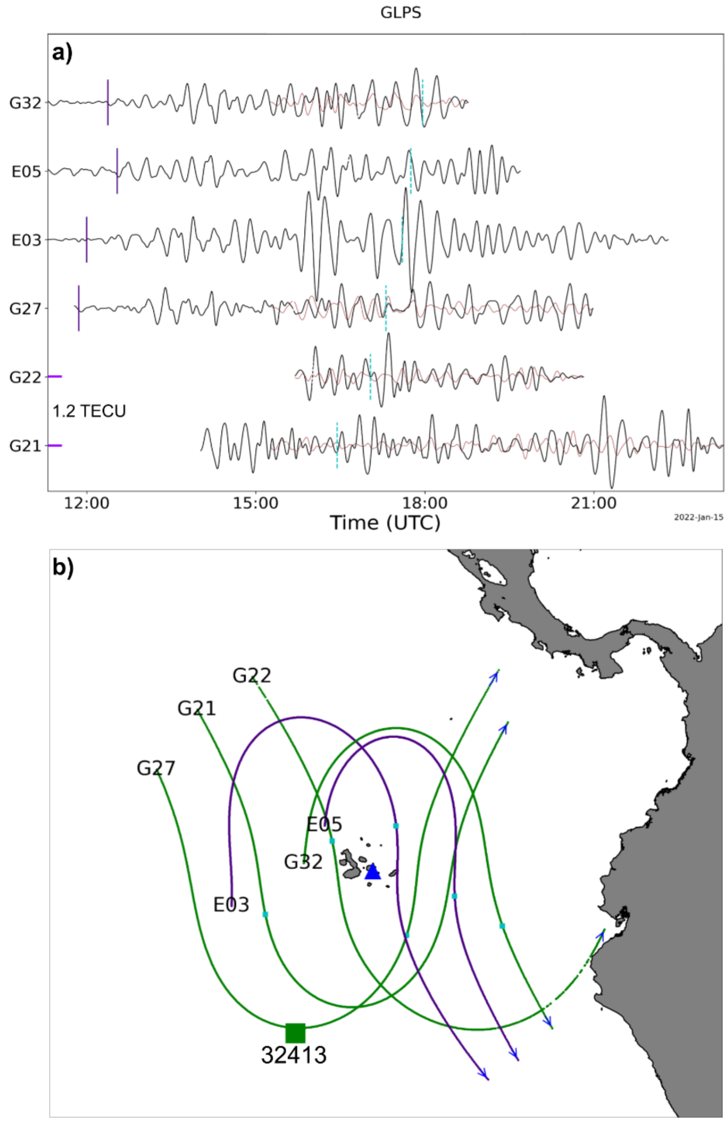

Figure S15. (a) The tsunami-induced ionospheric signatures detected in the vicinity of Galapagos Islands (GLPS GNSS receiver) following the passage of the tsunami triggered the HTHH volcanic eruption. **(b)** Geographic view of the GNSS receiver (red triangle) and the ionospheric tracks of the satellites whose sTEC time series are show in (a). The black square depicts the position of the tsunami buoy (DART 32413) used in Section 3.3 of the main text.

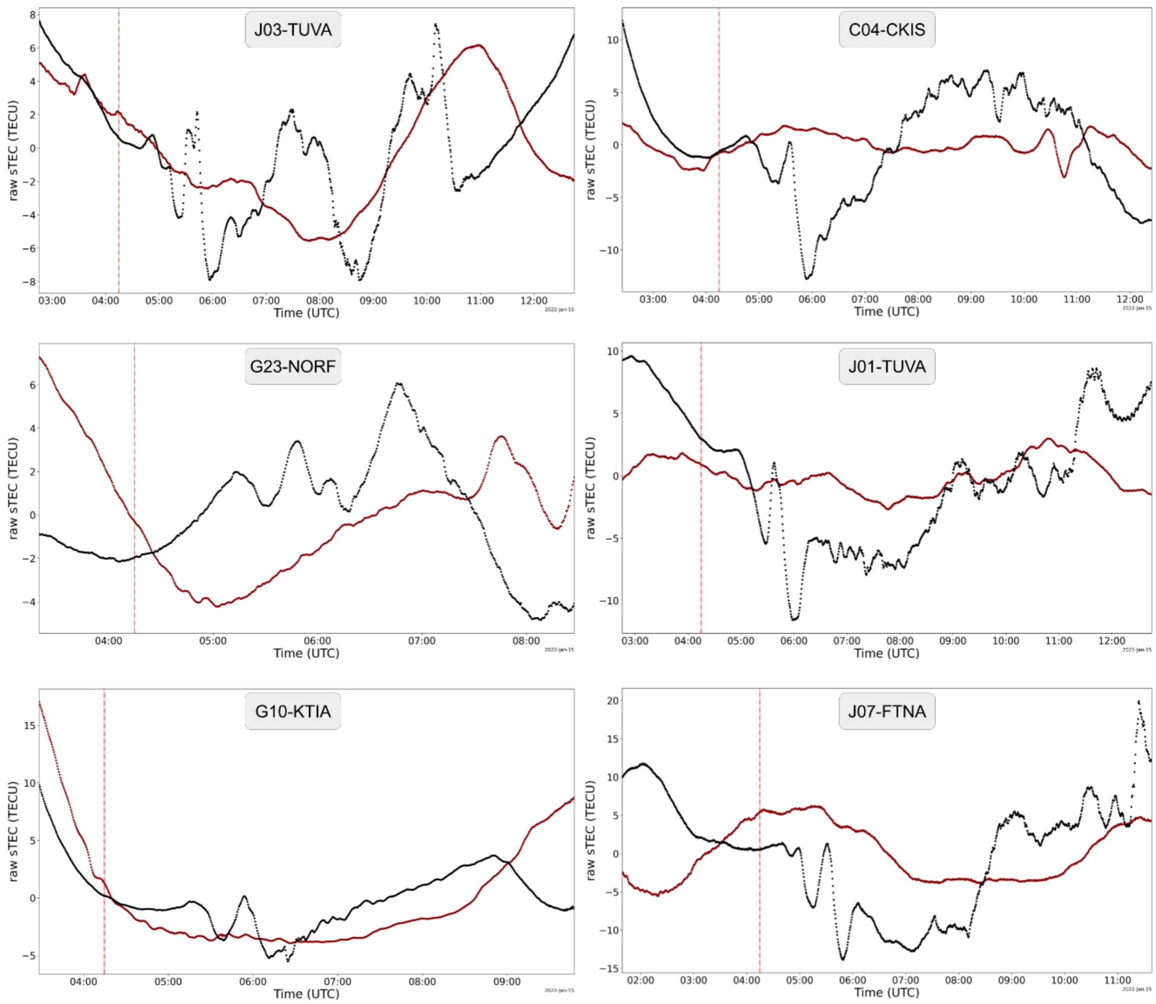

Figure S16. Raw ionospheric measurements during the eruption of the HTHH volcano to highlight the accompanied massive sTEC decreases and increases that resemble a large W-shape.

Contribution Statement:
Conceptualization: EM, LR
Methodology: EM, LR
Software: EM
Validation: EM, LR
Formal Analysis: EM
Investigation: EM, LR, AS
Writing - Original Draft: EM
Writing - Review and Editing: EM, LR, AS, BD
Visualization: EM
Supervision: LR, AS, BD

References

Artru, J., Ducic, V., Kanamori, H., Lognonné, P., & Murakami, M. (2005). Ionospheric detection of gravity waves induced by tsunamis. Geophys. J. Int, 160, 840–848. https://doi.org/10.1111/j.1365-246X.2005.02552.x

Calais, E., & Minster, J. B. (1995). Gps detection of ionospheric perturbations following the january 17, 1994, northridge earthquake. Geo-physical Research Letters, 22(9), 1045-1048. https://doi.org/10.1029/95GL00168

Davies, K., & Hartmann, G. K. (1997). Studying the ionosphere with the Global Positioning System. Radio Science, 32(4), 1695–1703. https://doi.org/10.1029/97RS00451

Davis, M. J. (1973). The integrated ionospheric response to internal atmospheric gravity waves. Journal of Atmospheric and Terrestrial Physics, 35(5), 929–959. https://doi.org/10.1016/0021-9169(73)90074-3

Donn, W. L., & Posmentier, E. S. (1964). Ground-coupled air waves from the great alaskan earthquake. Journal of Geophysical Research (1896-1977), 69(24), 5357-5361. https://doi.org/10.1029/JZ069i024p05357

Evans, J. V. (1957). The electron content of the ionosphere. Journal of Atmospheric and Terrestrial Physics, 11(3–4), 259–271. https://doi.org/10.1016/0021-9169(57)90071-5

Galvan, D. A., Komjathy, A., Hickey, M. P., & Mannucci, A. J. (2011). The 2009 Samoa and 2010 Chile tsunamis as observed in the ionosphere using GPS total electron content. Journal of Geophysical Research: Space Physics, 116(A6), n/a-n/a. https://doi.org/10.1029/2010JA016204

Hines, C. O. (1960). Internal atmospheric gravity waves at ionospheric heights. Canadian Journal of Physics, 38(11), 1441–1481. https://doi.org/10.1139/p60-150

Hines, C. O. (1972). Gravity Waves in the Atmosphere. Nature, 239 (5367), 73–78. https://doi.org/10.1038/239073a0

Hooke, W. H. (1969). E-region ionospheric irregularities produced by internal atmospheric gravity waves. Planetary and Space Science, 17(4), 749–765. https://doi.org/10.1016/0032-0633(69)90195-0

Liu, J. Y., Tsai, H. F., & Jung, T. K. (1996). Total Electron Content Obtained by Using the Global Positioning System. Terrestrial, Atmospheric and Oceanic Sciences, 7(1), 107. https://doi.org/10.3319/TAO.1996.7.1.107(A)

Liu, J. Y., Tsai, Y. B., Ma, K. F., Chen, Y. I., Tsai, H. F., Lin, C. H., . . . Lee, C. P. (2006). Ionospheric GPS total electron content (TEC) disturbances triggered by the 26 December 2004 Indian Ocean tsunami. Journal of Geophysical Research: Space Physics, 111 (5), 2–5. https://doi.org/10.1029/2005JA011200

Peltier, W. R., & Hines, C. O. (1976). On the possible detection of tsunamis by a monitoring of the ionosphere. Journal of Geophysical Research, 81(12), 1995–2000. https://doi.org/10.1029/jc081i012p01995

Ratcliffe, J. A. (1951). Some regularities in the F 2 region of the ionosphere. Journal of Geophysical Research, 56(4), 487–507. https://doi.org/10.1029/JZ056i004p00487

Ratcliffe, J. A. (1951). A quick method for analysing ionospheric records. Journal of Geophysical Research, 56(4), 463–485. https://doi.org/10.1029/JZ056i004p00463

Rolland, L. M., Occhipinti, G., Lognonn, P., & Loevenbruck, A. (2010). Ionospheric gravity waves detected offshore Hawaii after tsunamis. Geophysical Research Letters, 37(17). https://doi.org/10.1029/2010GL044479

Titheridge, J. E. (1972). Determination of ionospheric electron content from the Faraday rotation of geostationary satellite signals. Planetary and Space Science, 20(3), 353–369. https://doi.org/10.1016/0032-0633(72)90034-7

Zhang, S.-R., Fukao, S., Oliver, W. L., & Otsuka, Y. (1999). The height of the maximum ionospheric electron density over the MU radar. Journal of Atmospheric and Solar-Terrestrial Physics, 61(18), 1367–1383. https://doi.org/10.1016/S1364-6826(99)00088-7

Zhivetiev, I. (2019). gnss-tec (v1.1.1). https://github.com/gnss-lab/gnss-tec